THREE-DIMENSIONAL KINETIC SIMULATIONS OF ACTIVE SUSPENSIONS: EFFECT OF CHEMOTAXIS AND STERIC INTERACTION

BY

BARATH EZHILAN

THESIS

Submitted in partial fulfillment of the requirements
for the degree of Master of Science in Mechanical Engineering
in the Graduate College of the
University of Illinois at Urbana-Champaign, 2011

Urbana, Illinois

Adviser:

Professor David Saintillan

Abstract

In this work, the effects of chemotaxis and steric interactions in active suspensions are analyzed by extending the kinetic model proposed by Saintillan and Shelley [1, 2]. In this model, a conservation equation for the active particle configuration is coupled to the Stokes equation for the flow arising from the force dipole exerted by the particles on the fluid. The fluid flow equations are solved spectrally and the conservation equation is solved by second-order finite differencing in space and second-order Adams-Bashforth time marching.

First, the dynamics in suspensions of oxytactic run-and-tumble bacteria confined in thin liquid films surrounded by air is investigated. These bacteria modify their tumbling behavior by making temporal comparisons of the oxygen concentration, and, on average, swim towards high concentrations of oxygen. The kinetic model proposed by Saintillan and Shelley [1, 2] is modified to include run-and-tumble effects and oxygentaxis. The spatio-temporal dynamics of the oxygen and bacterial concentration are analyzed. For small film thicknesses, there is a weak migration of bacteria to the boundaries, and the oxygen concentration is high inside the film as a result of diffusion; both bacterial and oxygen concentrations quickly reach steady states. Above a critical film thickness (approximately 200 micron), a transition to chaotic dynamics is observed and is characterized by turbulent-like 3D motion, the formation of bacterial plumes, enhanced oxygen mixing and transport into the film, and hydrodynamic velocities of magnitudes up to 7 times the single bacterial swimming speed. The simulations demonstrate that the combined effects of hydrodynamic interactions and oxygentaxis create collective three-dimensional instabilities which enhances oxygen availability for the bacteria. Our simulation results are consistent with the experimental findings of Sokolov et al. [3], who also observed a similar transition with increasing film thickness.

Next, the dynamics in concentrated suspensions of active self-propelled particles in a 3D periodic domain are analyzed. We modify the kinetic model of Saintillan and Shelley [1, 2] by including an additional nematic alignment torque proportional to the local concentration in the equation for the rotational velocity of the particles, causing them to align locally with their neighbors (Doi and Edwards [4]). Large-scale three-dimensional simulations show that, in the presence of such a torque both pusher and puller suspensions are unstable to random fluctuations and are characterized by highly nematic structures. Detailed measures are

defined to quantify the degree and direction of alignment, and the effects of steric interactions on pattern formation will be presented. Our analysis shows that steric interactions have a destabilizing effect in active suspensions.

Acknowledgments

I extend my sincere thanks to my guide, Dr. David Saintillan, for his strong motivation and valuable guidance throughout the course of my research. I gratefully acknowledge the funding from the National Science Foundation and the computational facilities provided by the National Center for Supercomputing Applications. I thank Dr. Michael Shelley from the Courant Institute for the collaboration on concentrated active suspensions. The existence of a nematic basestate presented in section 3.3 was derived by him. I immensely thank Amir Alizadeh Pahlavan for providing me with his codes and answering my email queries when I was getting started. I thank all members of the Saintillan Research Group: Karthik, Jaesung, Hari, Deb, Shrenik, Tom for their support and encouragement. Special thanks to Jaesung Park for his advice and timely help.

Finally, I thank my friends and family for always believing in me, and encouraging me to pursue my goals.

Table of Contents

List of Figures

Chapter 1

Introduction

Collective motion is a spectacular phenomenon that has enthralled scientists across different fields for a long time. Simply put, it describes the complex, coordinated dynamics exhibited by a system consisting of interacting elements governed by simple laws. This phenomenon is ubiquitous in biology. Fishes swirl like a stirred fluid to escape from a nearby predator. Aerial display of birds, locust marching in a field, rotating colony of fire ants, collectively swarming bacteria are a few more examples [6]. Biologists study the phenomenon to provide functional explanation. Physicists study the mechanisms that lead to emergence of collective behavior. Computer scientists try to utilize the understanding of collective motion to design robots where simple interacting agents can perform complex tasks.

Dynamics in suspensions of micro-organisms (henceforth, called active suspensions) is one other fascinating instance of collective motion. Micro-organisms can be considered as polar rods that propel themselves by injecting energy into the surrounding medium. The terms: active particle/swimmer/self-propelled particle are used interchangably in this thesis to describe micro-organisms. Recent experiments in active suspensions have reported rich collective behavior characterized by complex pattern formation and density fluctuations [7, 8], higher swimming speeds [3], spatio-temporal coherence [9], 3D turbulent-like behavior [3, 8], nematic structures[5], enhanced passive tracer diffusivities [10, 11] and motion which takes the form of whirls, jets and vortices [12, 13]. In the collective state, individuals induce strong local flows in the fluid medium which influence the motion of other cells, leading to co-ordinated motion.

To understand the collective dynamics in active suspensions, it is first necessary to understand the motion of a single active particle. Micro-organisms have length and velocity scales of the order of microns, therefore, the Reynolds number given by $Re = \frac{UL}{\nu}$ is very small. This means that the inertial effects can be ignored in this regime. As a result, the net force on an active particle is zero, and any external force is directly transferred to the fluid medium. This means that the strategies used for locomotion by organisms like fish, birds, human beings does not help when $Re << 1$. At low Reynolds number, the fluid medium satisfies the Stokes equation which are linear and time-independent. As a consequence of these two properties, the aspects of low Reynolds number locomotion can be described by purely a geometric point of view [14, 15].

Another interesting property of low Reynolds number locomotion is described by the scallop theorem which states that a swimmer must deform in a way that is not invariant under time-reversal, to propel itself.

Micro-organisms have evolved different propulsion strategies like ciliary or flagellar locomotion to meet the constraints in the low Reynolds number regime. Irrespective of the mechanism employed by different swimmers, the hydrodynamics exhibits universal features. An active particle exerts a propulsive force $\mathbf{F}_p$ which is exactly balanced by the viscous drag ($\mathbf{F}_p = -\mathbf{F}_d$, because the particle is force-free). To leading order, this exerts a force dipole on the fluid medium. We introduce two types of swimmers: A pusher particle, which exerts thrust through its tail; A puller particle, which exerts thrust through its head. The force dipole exerted on the fluid is positive for pullers and negative for pushers.

While locomotion of single micro-organisms is well studied experimentally and theoretically, the exact mechanisms and functionality of such collective dynamics in large populations of micro-organisms remain unclear. Direct numerical simulations of these systems have been performed, using different models [16, 17, 18, 19]. These simulations have been successful in reproducing the experimental observations, but this approach is very expensive.

A simpler approach is kinetic modeling which involves developing continuum equations that govern the dynamics of active particles. The first kinetic model for active suspensions was developed by Ramaswamy et al. [20, 21, 22], who adapted the existing kinetic models for liquid crystals by including the effect of force dipoles in the Navier Stokes equation, and showed that aligned suspensions of self-propelled particles are unstable at long wavelengths for a specific range of wave angles. Other kinetic models have been proposed and the interested reader is referred to recent reviews [23, 24].

The work presented in this thesis is centered on the kinetic model proposed by Saintillan and Shelley [1, 2], where a conservation equation for the active particle is coupled with the Stokes equation for the local disturbance velocity (created by the force dipoles exerted by the active particles). Using numerical analysis and 2D simulations they showed that pusher suspensions were unstable to perturbations from the isotropic state while puller suspensions were stable. These instabilities were driven by the active stresses and a criterion for the onset of collective swimming due to hydrodynamic interactions was derived.

The analysis of Saintillan and Shelley [1, 2] considered the sole effect of hydrodynamic interactions. However, in reality, the motion of the swimming particles are influenced by several other effects. Micro-organisms swarm near surfaces and bias their motion towards an attractant or away from repellents by a process called chemotaxis. A fundamental understanding of how chemotaxis in confined environment affects the collective behavior in active suspensions has potential applications in pathogenesis of diseases caused by chemotactic bacteria, design of bacterial micromixers etc. Also, micro-organisms like bacteria usually swim

as concentrated populations where the steric effects between the swimmers become important. So, including steric interactions in the kinetic model and studying its effect on the collective behavior will help us provide a realistic description of the experimental observations.

1.1 Overview of the present work

In this work, we extend the Saintillan-Shelley model [1, 2] to include the effect of steric and chemotactic interactions. In Chapter 2, the dynamics in a suspension of oxytactic bacteria confined in thin films is investigated using 3D numerical simulations, where we report onset of large scale chaotic dynamics above a threshold film thickness as observed in recent experiments [3]. Detailed descriptions of the spatio-temporal evolution of both oxygen and bacterial fields are provided. In Chapter 3, we discuss the dynamics in concentrated active suspensions, and show that steric interactions lead to instabilities in both pusher and puller suspensions. Finally, conclusions are provided in Chapter 4.

Chapter 2

Oxygen transport and mixing dynamics in suspensions of Oxytactic bacteria

2.1 Introduction

Chemotaxis is the ability of a micro-organism to modulate its motion in response to changes in chemical concentration. This ability is important for micro-organisms to better exploit nutrients essential for their survival and to protect themselves from poisonous substances. When the interaction is attractive, chemotaxis leads to self-organization of the biological system into coherent structures [25].

Bacterial chemotaxis presents a powerful model system to understand how organisms sense and respond to chemical gradients [26]. Bacterial locomotion consists of motion along straight lines called "runs" interspersed by random reorientation called "tumbles" (Brown and Berg [27]). This behavior is called run-and-tumble motion. Bacteria perform chemotaxis by modulation of the tumbling frequency. Since the typical length of bacteria is of the order of μm,it is difficult for a micro-organism to measure spatial gradients. Instead, they sense changes in chemical concentration by making temporal comparisons with the recent past. When a bacterium is moving in the direction of increasing chemo attractant it decreases its tumbling frequency. Thus the straight runs lengthen in the direction of high oxygen concentration, thus on average, the bacteria moves towards higher chemo attractant concentration. When the bacteria biases its motion towards higher concentration of oxygen, it is called aerotaxis. Aerotactic bacteria also consume oxygen and thereby they create the oxygen gradients themselves. This, when coupled to the aerotactic bias, leads to interesting dynamics [28] characterized by pattern formation and swimming towards free surfaces. About a decade ago, such dynamics were attributed to bioconvection. Bioconvection is a mechanism similar to Rayleigh-Benard convection, where an overturning instability occurs when bacteria denser than water swim (on average) upward because of aerotaxis [29] or other factors.

Keller and Segel [30] proposed a model for chemotaxis, which is recognized as the Keller-Segel model. This model consists of two coupled advection-diffusion equations that govern the evolution of number density of biological cells and evolution of the chemoattractant. This model and its variations have been used by several researchers [31] to study the effect of chemotactic interactions in bacterial suspensions. Pedley and

Kessler [28] and Hill and Pedley [29] present a thorough review of the analytical treatment of bioconvection.

However, bioconvection occurs only above a critical Rayleigh number, and the associated length scale is in the order of metres [32]. In this work, we focus on collective motion at much smaller scales where bioconvection is not relevant. Recent experiments of Sokolov et al. [3] is the main motivation to consider this problem.

Sokolov et al. [3] recently studied the dynamics of aerotactic bacteria in free-standing films for different film thicknesses. They observed that above a critical film thickness, the spatially homogeneous self-organized bacterial motion transitions to a three-dimensional chaotic state characterized by spontaneous formation and break-up of dense bacterial plumes. This transition coincides with the onset of a bacterial depletion zone at the center of the film. It was pointed out that the Rayleigh numbers for these experiments were 2 orders of magnitude smaller than the critical value for the onset of bioconvection, and the observed collective motion was attributed to oxygentaxis.

Recent theoretical and experimental studies have suggested a hydrodynamic origin of large scale collective motion in suspensions of swimming micro-organisms [8, 1, 2, 33]. So, it would be interesting to see if we can explain the dynamics observed in the experiments of Sokolov et al. [3] based on hydrodynamic interactions or a coupled effect of oxygentaxis and hydrodynamic interactions.

In section 2.2, we extend the kinetic model, previously introduced by Saintillan and Shelley [1, 2] to model chemotaxis in suspensions of rod-like run-and-tumble swimmers. In section 2.3, we perform 3D numerical simulations, analyze the spatio-temporal dynamics and show that our results are in agreement with the experimental predictions of Sokolov et al [3].

2.2 Kinetic Model

2.2.1 Smoluchowski equation for the conservation of active particles

We represent the active particles using a distribution function $\Psi(\mathbf{x}, \mathbf{p}, t)$. This function measures the probability of finding a particle in a center-of-mass position $\mathbf{x}$, oriented along the unit vector $\mathbf{p}$, which describes the swimming direction. This distribution function satisfies a conservation (or Smoluchowski) equation [4].

$$\frac{\partial \Psi}{\partial t} = \left[-\lambda\Psi + \int_{\Omega} T(\mathbf{p}, \mathbf{p}'; \delta)\Psi'\lambda' d\mathbf{p}' \right] - \nabla_x \cdot (\dot{\mathbf{x}}\Psi) - \nabla_p \cdot (\dot{\mathbf{p}}\Psi). \tag{2.1}$$

The bracketed terms of Eq. (2.1) accounts for the run-and-tumble behavior of the swimmers. The first term $\lambda\Psi(\mathbf{x}, \mathbf{p}, t)$ accounts for the active particles that have stopped swimming along the direction $\mathbf{p}$ because

of tumbling (λ represents the tumbling frequency). $T(\mathbf{p}, \mathbf{p}'; \delta)$ describes the probability that a swimming particle tumbles from an orientation $\mathbf{p}'$ to $\mathbf{p}$. So, the second term accounts for the swimming particles that have tumbled from other orientations to swim along the direction $\mathbf{p}$.

The particle fluxes $\dot{\mathbf{x}}$ and $\dot{\mathbf{p}}$ in Eq. (2.1) are modeled as

$$\dot{\mathbf{x}} = V_0\mathbf{p} + \mathbf{u} - D\,\nabla_x(\ln\Psi) \tag{2.2}$$

$$\dot{\mathbf{p}} = (\mathbf{I} - \mathbf{pp}) \cdot [\nabla_x \mathbf{u} \cdot \mathbf{p}] - d\,\nabla_p(\ln\Psi) \tag{2.3}$$

The center of mass flux in Eq. (2.2) accounts for the translational motion of the active particle.This is expressed as a sum of self propulsion velocity $V_0\mathbf{p}$, advection by the local fluid velocity $\mathbf{u}(\mathbf{x}, t)$, and center-of-mass diffusion with a constant isotropic diffusivity D. Similarly, Eq. (2.3) accounts for particle rotation under the effect of the local velocity gradient via Jeffery's equation [34, 35]. Rotational diffusion is also included with constant diffusivity d.

As noted in section 2.1 the swimming particle modifies its tumbling frequency in response to changes in concentration of oxygen that they sample as they swim. This tumbling bias leads to oxygentaxis, and is accounted by Eq. (2.4) where ξ is the oxytactic response strength.

$$\lambda = \lambda_0 \exp(-\xi Ds/Dt) \text{ where } \frac{Ds}{Dt} = \frac{\partial s}{\partial t} + (\mathbf{p} + \mathbf{u}) \cdot \nabla_x s \tag{2.4}$$

This expression for the tumbling frequency is a generalization of the expression used by Bearon and Pedley [36] (whose analysis considered steady linear gradients of chemoattractants). It should be noted that Chen et al [37] also modeled the tumbling frequency in a similar fashion.

The probability distribution function can be normalized as $\frac{1}{V}\int_V d\mathbf{x} \int_\Omega d\mathbf{p}\Psi(\mathbf{x}, \mathbf{p}, t) = n$. Here, $n = N/V$ denotes mean number density of the suspension, where N is the total number of swimming particles.

To close Eqs. (2.1), (2.2) and (2.3), the fluid velocity $\mathbf{u}$ and the evolution of the oxygen concentration s must be described.

2.2.2 Stokes equation for the local disturbance velocity

In the low-Reynolds-number regime relevant to the locomotion of microorganisms, the disturbance fluid flow created by the particles satisfies the Stokes equations

$$\nabla_x q - \mu\nabla_x^2 \mathbf{u} = \nabla_x \cdot \mathbf{\Sigma}^p, \quad \nabla_x \cdot \mathbf{u} = 0, \tag{2.5}$$

where μ is the viscosity of the suspending fluid, and q is the fluid pressure. In Eq. (2.5), $\mathbf{\Sigma}^p(\mathbf{x},t)$ is the particle extra stress, obtained as the orientational average of the force dipoles exerted by the particles on the fluid

$$\mathbf{\Sigma}^p(\mathbf{x},t) = \sigma_0 \int_\Omega \Psi(\mathbf{x},\mathbf{p},t)\mathbf{pp}\, d\mathbf{p}, \tag{2.6}$$

where the strength of the dipole resulting from self propulsion σ_0 is a constant whose sign depends on the mechanism for swimming: head-actuated swimmers or pullers, such as the alga *Chlamydomonas*, result in $\sigma_0 > 0$, whereas rear-actuated swimmers or pushers, such as most swimming bacteria including *E. Coli* and *B. Subtilis*, result in $\sigma_0 < 0$. In addition, σ_0 is related to the single-particle swimming speed U_0 and particle length l by a relation of the form $\sigma_0/\mu U_0 l^2 = \alpha$, where α is a dimensionless $O(1)$ parameter with the same sign as σ_0.

2.2.3 Evolution of oxygen

The evolution of the oxygen field $s(\mathbf{x},t)$ also can be described considering its convection by the disturbance velocity field $\mathbf{u}$, consumption by the swimmers and diffusion as shown below

$$\frac{\partial s}{\partial t} + \mathbf{u}(\mathbf{x},t)\cdot\nabla_x s - D_o\nabla_x^2 s = -\kappa c(\mathbf{x},t) f(s(\mathbf{x},t)) \tag{2.7}$$

in which D_o is the oxygen diffusion constant, κ is the rate of oxygen consumption by a single bacterium (in oxygen rich environments), and $c = \int_\Omega \Psi\, d\mathbf{p}$. A function $f(x) = \left(\frac{x-0.1}{0.9}\right)^{0.2}$ is included in the consumption term to account for the fact that the bacterial consumption ceases when the concentration of oxygen falls below 10 percent of its saturation value in a fluid medium.

2.2.4 Non-Dimensionalization

The coupled system of Eqs. (2.1)–(2.7) can be made dimensionless using the following characteristic length, velocity, and time scales: $l_c = (nl^2)^{-1}$, $u_c = V_0$, and $t_c = l_c/u_c$. The oxygen concentration is normalized by its value at the boundary. Upon non-dimensionalization, the only remaining parameters in the set of equations are the dimensionless stress magnitude α, the shape parameter γ, the diffusivities D, d and D_0; the tumbling frequency λ, oxytactic response strength ξ, and oxygen consumption coefficient κ. Therefore, the dependence on the number density would be through the system size, which is made dimensionless by $(nl^2)^{-1}$. We choose values for the non-dimensional parameters which are close to that of the experiments of Sokolov et al [3] to compare results from our model to their experimental observations.

2.3 Numerical Simulation

Three dimensional numerical simulations are performed by integrating the kinetic equations described in section 2.2 by using spectral solutions for the Stokes equation, second-order finite differences for the flux terms and second-order Adams-Bashforth time-marching for the Smoluchowski equation. It should be noted that the kinetic model has 5 independent variables (x, y, z, θ, ϕ), making the simulations computationally expensive. Hence, the simulations were carried out in parallel, using 64 processors [38].

We consider the dynamics in a doubly periodic domain (periodic in x and z directions). The surface of the film is perpendicular to the y-direction. $y = 0$ and $y = L$ correspond to the boundary planes for a film of thickness L. In the y-direction, we use a free-shear stress boundary condition for the velocity given by Eq. (2.8) and zero net probability flux boundary condition for the bacterial distribution function given by Eq. (2.9).

$$\hat{\mathbf{y}} \cdot \nabla_x \mathbf{u}(\mathbf{x}, t) = 0 \text{ at y=0,L} \tag{2.8}$$

$$\hat{\mathbf{y}} \cdot \int_\Omega \dot{\mathbf{x}} d\mathbf{p} = 0 \text{ at y=0,L} \tag{2.9}$$

These boundary conditions are satisfied by using a reflection condition for the distribution function. For the oxygen field, we have $s = 1$ at the boundaries.

We start with a uniform isotropic bacterial concentration. At t=0, the oxygen concentration inside the film is taken to be zero. We introduce random perturbations to the bacterial distribution and study the spatio-temporal dynamics of the bacterial number density, oxygen concentration and local disturbance velocity. Simulations are performed for several different film thicknesses, ranging from 50-600 microns.

As the simulations start, oxygen diffuses into the film from the boundaries and the bacteria start to consume the oxygen. Both these effects create gradients of oxygen inside the film. The bacteria modify their run-and-tumble behavior to preferentially move towards the higher oxygen concentration and this leads to the migration of bacteria towards the boundaries.

Our simulations show that steady states are reached for smaller film thicknesses, but beyond a threshold concentration, there is a transition to chaotic 3D dynamics. This can be seen from Fig. 2.1 and Fig. 2.2 which shows bacterial and oxygen field in 100 and 500 micron films.

We classify the dynamics into 3 different regimes based on the film thickness.

Regime I: We find that, in films of thickness $\leq$ 100 micron, the bacterial number density and oxygen concentration quickly reach steady states where the bacterial and oxygen profiles are uniform along x and z.

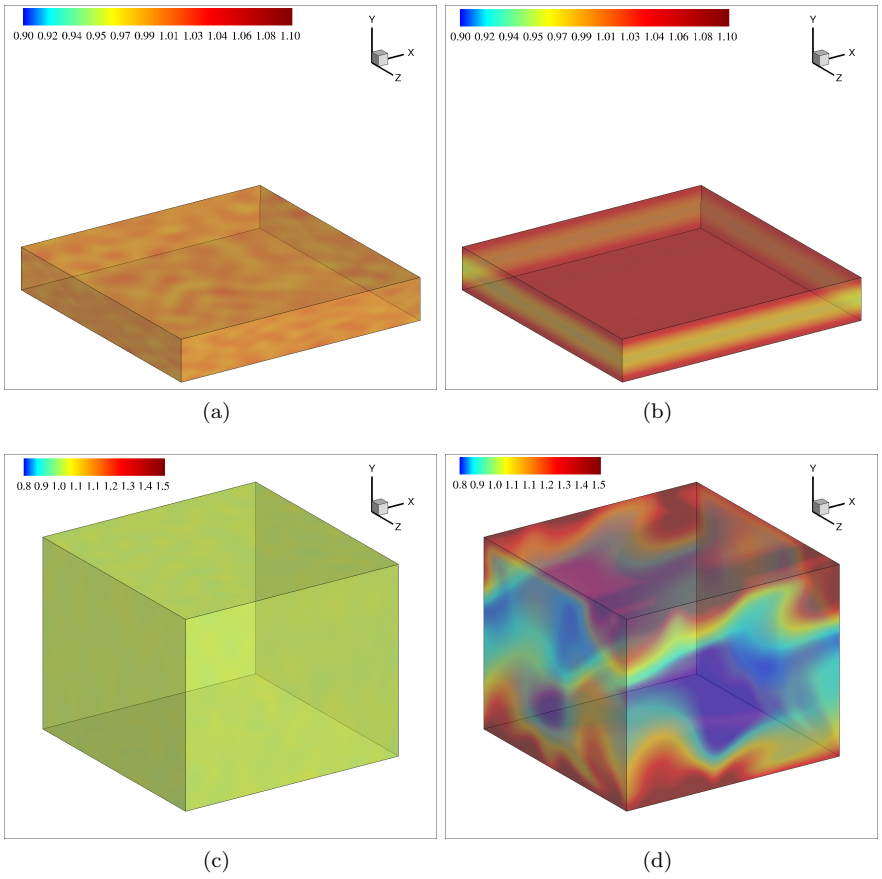

Figure 2.1: Bacterial number density field: a) $t = 0$, Channel size $100\mu m$; b) $t = 60$ sec, $100\mu m$; c) $t = 0$, Channel size $500\mu m$; b) $t = 60$ sec, $500\mu m$

There is a weak migration of bacteria to the boundaries. This is because of the high availability of oxygen inside the film because of diffusion. Bacteria can find the oxygen that they need within the film.Therefore, the tendency to swim towards the boundary is weak.

Regime II: For films of thickness, 200-400 micron, we observe large scale three dimensional flows, chaotic motion, number density fluctuations, and several other interesting collective features. The striking feature in this regime is that bacteria which migrate to the boundaries in search of oxygen, travel back into the center of the film, taking the form of high density plumes, and this, we suggest, leads to the enhancement of availability of oxygen in the center of the film.

Regime III: For films of thickness greater than 400 micron, we observe a marked change in the dynamics, characterized by the formation of an oxygen depletion layer in the center of the film, stronger bacterial plumes and enhanced y-velocities.

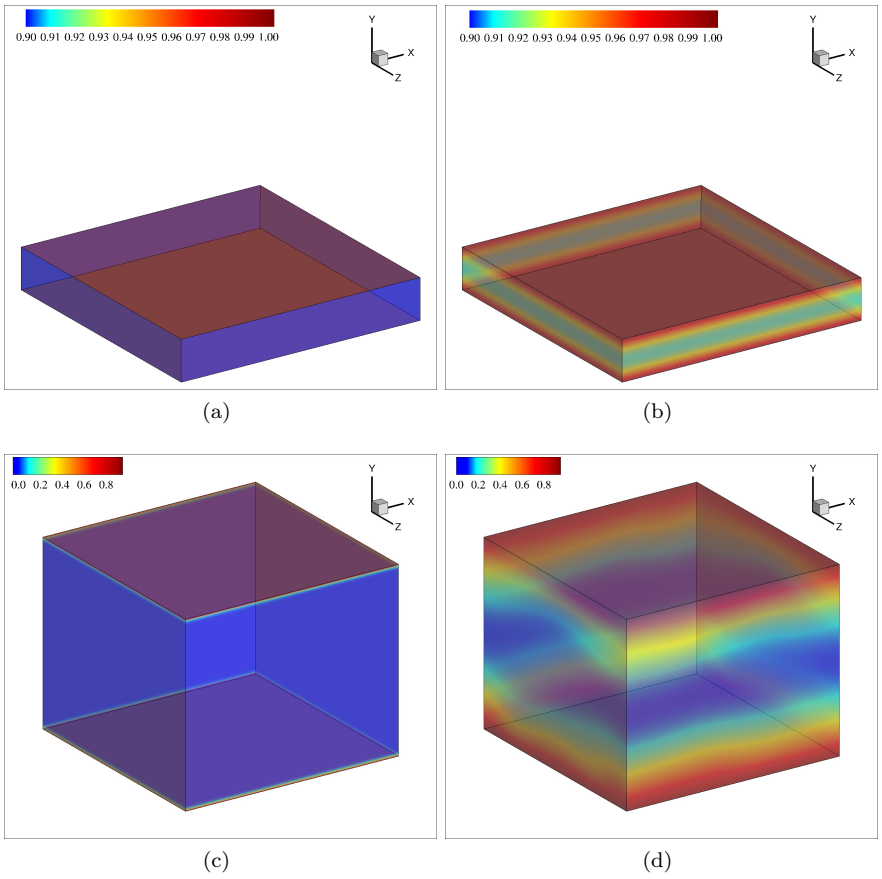

Figure 2.2: Oxygen concentration field: a) $t = 0$, Channel size $100\mu m$; b) $t = 60$ sec, $100\mu m$; c) $t = 0$, Channel size $500\mu m$; b) $t = 60$ sec, $500\mu m$

2.3.1 Time-averaged dynamics

In this section, we discuss the variation of the various fields across the film by averaging them over time, and along the directions x and z.

We find it useful to compare the dynamics with a basestate corresponding to a steady bacterial concentration uniform along x and z axis. We evaluate this basestate by allowing the probability distribution function to vary only as a function of y and θ ($\Psi = \Psi(y, \theta)$) and the oxygen concentration to vary only as a function of y ($s = s(y)$).Such a profile doesn't create a local disturbance velocity. This comparison gives us important information on the effects of large scale collective motion in the dynamics of the suspension.

Fig. 2.3 shows the time-averaged profiles of bacterial number density and oxygen concentration averaged over x, z and t. We see that for the smallest thickness (100 micron), the film is oxygen rich, oxygen concentration is almost uniform in the y-direction and hence the migration of bacteria to the boundaries is weak.

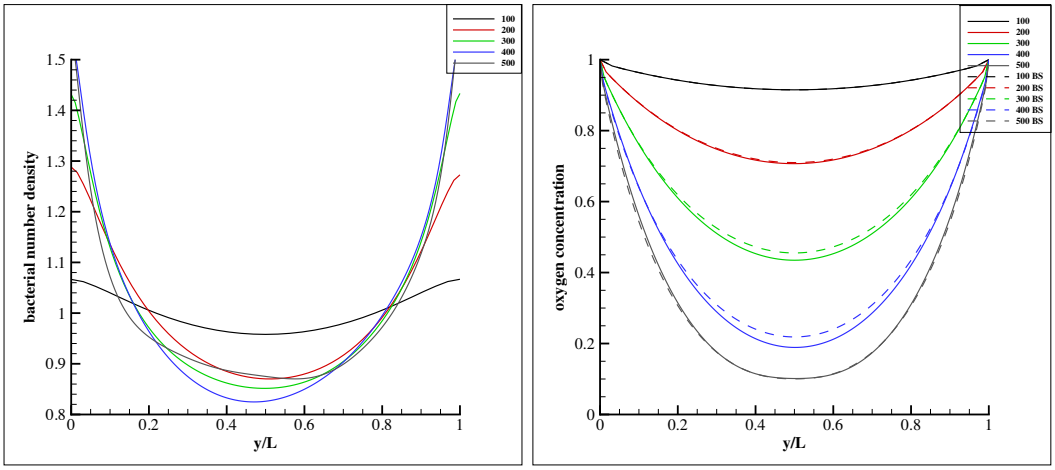

(a) (b)

Figure 2.3: a) Bacterial number density b) Oxygen concentration

For higher thickness (200 to 400 micron), the oxygen gradients in the y-direction become increasingly stronger. This drives the migration of bacteria to the boundary. As film thickness increases, the migration to the boundaries and depletion of bacteria in the center of the film becomes more pronounced.

In films of thickness $\gtrsim$ 400 micron, there is a oxygen depletion layer formed in the center of the film. Oxygen depletion layer is a region where s $<$ 0.1 where the bacteria stops consuming oxygen. For the 500 micron curve in 2.3 (b), the depletion layer is 100 micron thick (the flat part of the profile from y/L = 0.4 to 0.6). In this oxygen depletion layer, the spatial gradients of oxygen are virtually absent, therefore, the bacteria in this zone do not perform oxygentaxis. Hence, the bacteria traveling from the film boundaries and entering this depletion zone becomes incapable of using oxygentaxis to migrate back to the boundaries. This causes a marked change in the shape of the number density profile when compared to the profiles for regime II (200-400 micron) as can be seen in 2.3 (a), where the bacterial number density is higher in the center for 500 micron. It should be noted that Sokolov et al. [3] also reported a similar characteristics in a 530 micron film (where they observed that a stagnant zone of non-motile bacteria was formed in the center of the film).

We now look into the rate of oxygen consumption across the thickness of the film. This is obtained by averaging the consumption term (R.H.S) in the oxygen evolution equation over x, z and t as shown in Eq. (2.10).

$$\text{oxygen consumption rate}(y) = \langle c(\mathbf{x},t) f(s(\mathbf{x},t)) \rangle_{x,z,t} \tag{2.10}$$

From Fig. 2.4, we find that oxygen consumption is almost uniform across the thickness of the film in

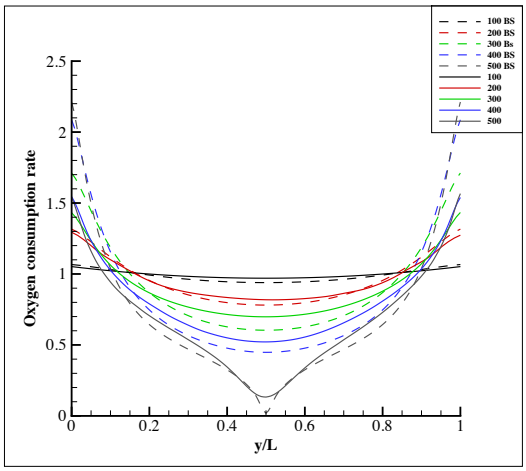

(a)

Figure 2.4: Oxygen consumption rate

regime I, which is expected because of uniform bacterial and oxygen profiles. As thickness is increased in regime II from 200 to 400 micron, the oxygen consumption by the bacteria increases near the boundaries and decreases inside the film. In regime III, the curves change in shape, and the inflection point characterizes the onset of the depletion layer, within which the oxygen consumption reduces drastically.A comparison with the basestate profile shows that collective motion significantly reduces the oxygen consumption near the boundary and enhances the oxygen consumption inside the film.

Fig. 2.5 shows the variation of the velocity components across the film thickness. A measure of the average velocity is given by Eq .(2.11)–(2.14)

$$v_x(t) = \left\langle u_x^2 \right\rangle^{0.5} \tag{2.11}$$

$$v_y(t) = \left\langle u_y^2 \right\rangle^{0.5} \tag{2.12}$$

$$v_z(t) = \left\langle u_z^2 \right\rangle^{0.5} \tag{2.13}$$

$$v(t) = \left\langle |u|^2 \right\rangle^{0.5} \tag{2.14}$$

$v_x(t)$,$v_z(t)$,$v(t)$ show similar variations characterized by a constant profile for regime I, and a parabolic curve deepening with increasing film thickness for regime II and III.

The temporal dynamics of the y-velocity is more interesting. We find that the y-velocity is zero for regime I. In regime II, the profile looks like a downward parabola, which gets progressively flattened at the center, with film thickness. The pronounced 3 dimensionality of the disturbance flow in larger films is confirmed by the higher values of y-velocity for larger film thickness, and this leads to the generation of

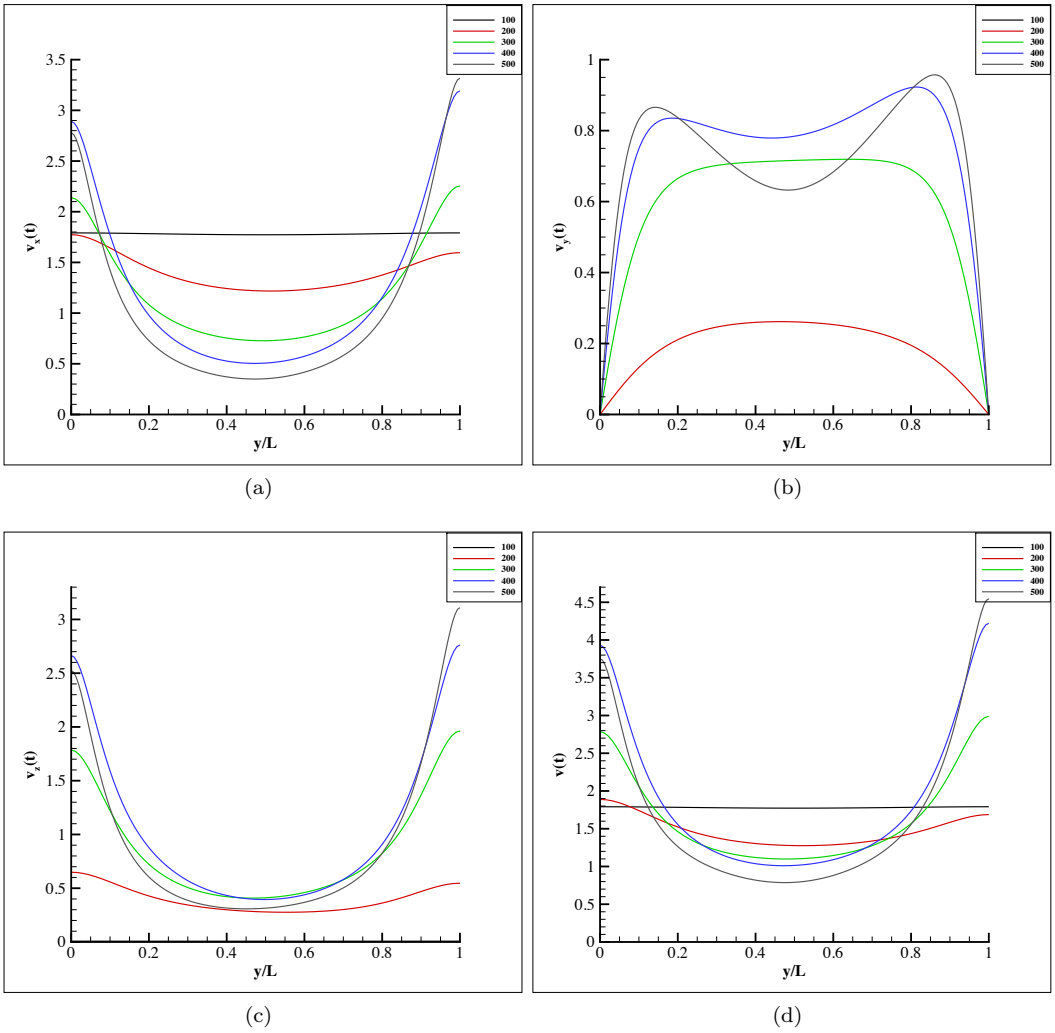

Figure 2.5: Average velocity a) x-velocity; b) y-velocity; c) z-velocity; d)velocity magnitude

bacterial plumes for this case. However, for 400 micron and beyond (regime III), the shape of the profile changes, with depression in the center of the film. This effect needs further investigation.

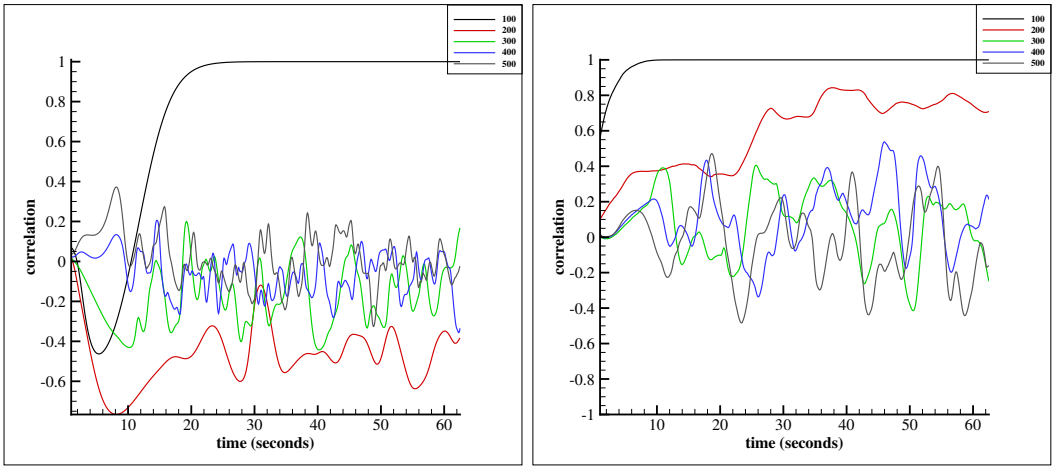

(a) (b)

Figure 2.6: Correlation of a) bacterial number density b) local disturbance velocity between top and bottom boundaries

2.3.2 Time dynamics

The correlation of bacterial number density and local disturbance velocity between top and bottom boundaries is given by Eq .(2.15) and Eq .(2.16) and their temporal evolution is shown in Fig. 2.6.

$$c_{nd}(t) = \frac{\left\langle \left(c_{top} - \langle c_{top}\rangle_{x,z}\right) \times \left(c_{bot} - \langle c_{bot}\rangle_{x,z}\right) \right\rangle_{x,z}}{\left(\left\langle \left(c_{top} - \langle c_{top}\rangle_{x,z}\right)^2 \right\rangle_{x,z} \left\langle \left(c_{bot} - \langle c_{bot}\rangle_{x,z}\right)^2 \right\rangle_{x,z} \right)^{\frac{1}{2}}} \tag{2.15}$$

$$c_{vel}(t) = \frac{\left\langle \mathbf{u}_{top} \cdot \mathbf{u}_{bot} \right\rangle_{x,z}}{\left(\left\langle |\mathbf{u}_{top}|^2 \right\rangle_{x,z} \left\langle |\mathbf{u}_{bot}|^2 | \right\rangle_{x,z} \right)^{\frac{1}{2}}} \tag{2.16}$$

In regime I, we find perfect correlation for both concentration, velocity at the center of the film. For 200 micron films, we find that velocities are positively correlated while concentration is anti-correlated, so we suspect that, this is a transition case that lies between the regime I and regime II. For all larger thicknesses, the dynamics is uncorrelated between top and bottom boundaries which confirms the three dimensional nature of the flow.

The temporal evolution of the oxygen field is investigated in Fig. 2.7. Fig. 2.7 (a) shows the flux of the oxygen into the field. This is defined as

$$\text{oxygen flux} = \left\langle \left| \frac{\partial s}{\partial y} \right|_{top} + \left| \frac{\partial s}{\partial y} \right|_{bot} \right\rangle_{x,z} \tag{2.17}$$

Initially the flux of oxygen is greatest due to the lack of oxygen in the field. The oxygen diffuses into the film and the bacteria start consuming the dissolved oxygen and migrating towards higher oxygen concentration

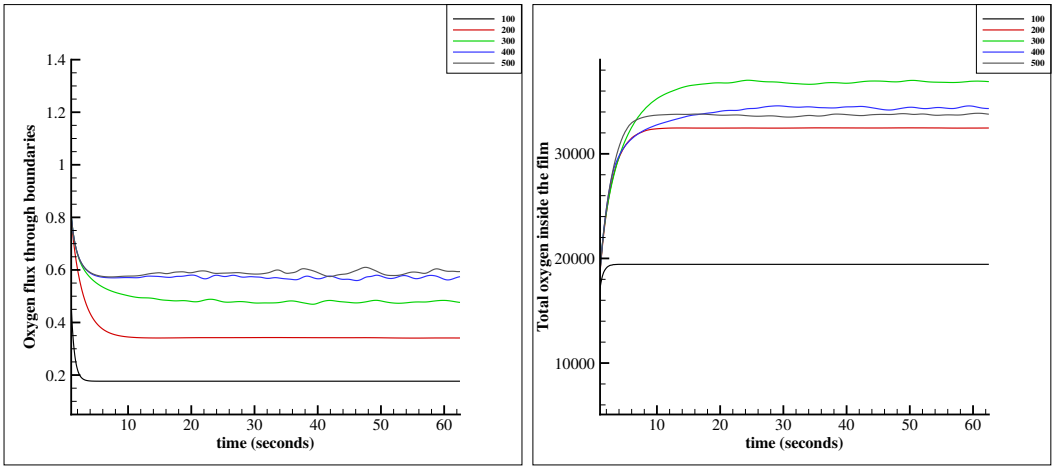

(a) (b)

Figure 2.7: a)Oxygen flux into the channel b) Total oxygen inside the film

until the system reaches to a statistically-steady state where consumption balances diffusion. The oxygen flux for lower thicknesses (i.e. $100, 200\mu m$ films) reaches a steady state value, which increases with the thickness of the film as the population of bacteria increases. However, as the instabilities become 3D for $300 - 500\mu m$ films, the flow mixes the oxygen from the interfaces into the film, thus making the oxygen flux to oscillate in time while again reaching to a statistically-steady state at long times.

The total amount of dissolved oxygen in the field. is shown in Fig. 2.7 (b).

$$\text{total oxygen inside the film}(t) = \langle s \rangle_{x,y,z} \tag{2.18}$$

It shows that the level of the oxygen in the field increases in time until it reaches an equilibrium state and this plateau level also increases with the film thickness as the population of the bacteria and the film volume increases.

2.4 Concluding Remarks

We have extended the kinetic theory of Saintillan and Shelley [1, 2] to model chemotaxis in suspension of swimmers undergoing run-and-tumble motion. By choosing appropriate values for the parameters, we have used this model to study the dynamics in a bacterial suspension confined in thin films. Using three-dimensional kinetic simulations, we observed a transition to chaotic motion beyond a critical film thickness, which is consistent with the recent experimental observations of Sokolov et al. [3]

Moreover, we characterized the dynamics by classifying it into 3 regimes: Regime I, when film thickness is

less than 100 micron, where the bacterial and oxygen fields reach a stable steady state, that is uniform along x and z directions; Regime II, when film thickness is in the range 200-400 micron, where three-dimensional chaotic motion is observed and is characterized by dense bacterial plumes; Regime III, when the film thickness is greater than 400 micron, where the dynamics is characterized by the formation of an oxygen depletion region in the center of the film, enhancement in the magnitude of hydrodynamic velocities and pronounced occurence of bacterial plumes.

Our simulations have successfully reproduced the experimental findings of Sokolov et al. [3]. Our analysis has also provided several new insights and key information on how the oxygen consumption, active power input, hydrodynamic velocities change due to the chaotic dynamics.

However, the mechanism behind these instabilities remain unclear. One important question remains to be answered: 'Is the instability purely a hydrodynamic effect or a combination of hydrodynamic and chemotactic effects?'.

Saintillan and Shelley [2] showed using linear stability analysis in a 3D periodic domain that instabilities occur only when the size of the simulation box (for a given concentration) exceeds a critical value. If we assume the instability as purely a hydrodynamic effect, this might be an explanation for the onset of large scale collective dynamics beyond a threshold film thickness. However, when chemotaxis was switched off in our simulations, we observed that no instability occur and the isotropic state is stable. This clearly indicates that oxygentaxis is necessary for instabilities to occur. So, it is safe to claim that the instability is a combined effect of hydrodynamic interactions and oxygentaxis. Whether the effect of oxygentaxis is to just augment the hydrodynamic instability driven by active stresses (which causes proliferation of oscillations in swimmer direction [39]) or provide new mechanisms for concentration fluctuations and large scale motion, needs to be further explored.

We speculate that, the instabilities occur when the strength of the oxygen gradients becomes higher than a critical value, which in our simulations and in the experiments of Sokolov et al. [3], happens when the film thickness becomes greater than 200 micron. Such an instability would be associated with the ability of the bacteria to orient in a preferrential direction due to oxygentaxis. Analytical treatment of the evolution Eqs. (2.1)-(2.7) will throw more light on these instabilities.

Chapter 3

Dynamics of concentrated active suspensions

3.1 Introduction

While analyzing the interactions between slender rod-like polymers (with diameter b and length L) at finite concentration, Doi and Edwards [4] divided the polymer solutions into 4 concentration regimes.

- **Dilute solution**: A solution whose concentration is low enough that the average distance between the polymers $n^{-\frac{1}{3}}$ is much larger than the length of the polymer L or

$$n \lesssim n_1 \approx \frac{1}{L^3} \tag{3.1}$$

  where n is the number of particles per unit volume. In this regime, each polymer rotates freely without being influenced by other polymers (hydrodynamic and steric interactions are neglible).

- **Semi-dilute solution**: At concentrations corresponding to $n \gg n_1$, the rotation of the polymer is restricted due to the effect of other polymers, but the static properties are not affected seriously until the concentration reaches another characteristic concentration n_2. This concentration regime, Semi-dilute, occurs for a concentration n that satisfies the equation below.

$$n_1 \lesssim n \ll n_2 \approx \frac{1}{bL^2} \tag{3.2}$$

  In this regime the excluded volume effects are negligible but the hydrodynamic interactions are significant and have to be taken into account.

- **Concentrated isotropic Solutions**: When the concentration n becomes greater than n_2, the excluded volume effects become important and the polymer align nematically with their neighbours because of steric interactions. But the solution remains isotropic till the concentration increases beyond another critical value n^* which is of the order of $\frac{1}{bL^2}$. This concentration regime occurs when

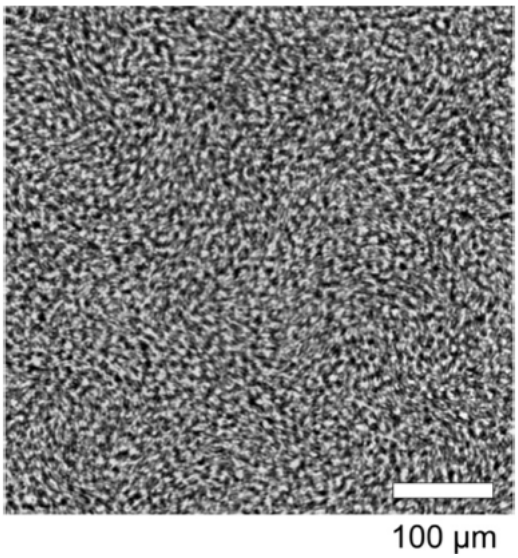

Figure 3.1: Zooming Bio Nematic phase Cisneros et al. [5]

$$n_2 \lesssim n \lesssim n^* \tag{3.3}$$

Even though the solution is macroscopically isotropic, steric interactions influences static and dynamical properties and have to be taken into account.

- **Liquid crystalline solution**: When concentration n becomes greater than n^*, the polymers align on a macroscopic scale in equilibrium (without any external field) and the solution becomes anisotropic. This occurs when

$$nbL^2 \geqslant 1 \tag{3.4}$$

Kinetic theories employed for modeling active suspensions (Saintillan and Shelley [1, 2], Subramanian and Koch [33]) describe active matter in the semi-dilute regime i.e., they account for hydrodynamic interactions and exclude steric interactions. One of the key findings of these kinetic models is that pusher suspensions showed instabilities and large scale flows while pullers were stable to perturbations in the isotropic state. The stability of puller suspensions is yet to be confirmed experimentally.

However, most experiments which report collective motion in active suspensions used a high concentration of swimmers. For example, Sokolov et al. [3] who reported collective motion in suspensions of *Bacillus subtilis* (diameter $0.7\mu m$, length $4\mu m$) containing 2×10^{16} cells per m^3. $nbL^2 = 0.224$ for these experiments, where the semi-dilute assumption is invalid.

Cisneros et al. [5] studied the dynamics in suspensions of *Bacillus subtilis* by varying the concentration. They observed no significant collective motion in the dilute and semi-dilute regime, but beyond a critical concentration, they observed a collective phase called zooming bionematic (shown in 3.1), characterized by highly nematic structures, high local swimming speeds. These structures form because of local ordering of the bacteria at higher concentration. They also noted that regions of high degree of alignment had larger number density.

These experimental studies are the main motivation to consider this problem. Steric interactions are important and have to be taken into account to be able to meaningfully describe collective motion observed in experiments. In section 3.2, we present the kinetic model for concentrated active suspensions which accounts for both steric and hydrodynamic interactions. In section 3.3, we probe the existence of a nematic basestate in the concentrated regime. In section 3.2, we present and analyze the results from the three-dimensional kinetic simulations of concentrated active suspensions, show that steric interactions have a destabilizing effect and both puller and pusher suspensions exhibit instabilities and large-scale flows.

3.2 Kinetic model

We extend the kinetic model developed by Saintillan and Shelley [1, 2] for semi-dilute active suspensions by including a nematic torque that accounts for steric interactions.

The distribution function of the active particles, Ψ (introduced in section 2.1) satisfies

$$\partial_t \Psi + \nabla_x \cdot (\dot{\mathbf{x}}\Psi) + \nabla_p \cdot (\dot{\mathbf{p}}\Psi) = 0, \tag{3.5}$$

and the translational and rotational fluxes are given by

$$\dot{\mathbf{x}} = V_0\mathbf{p} + \mathbf{u}(\mathbf{x}) - D\nabla_x(\log\Psi), \tag{3.6}$$

$$\dot{\mathbf{p}} = (\mathbf{I} - \mathbf{pp}) \cdot \nabla_x\mathbf{u} \cdot \mathbf{p} - d\nabla_p(\log\Psi) - \nabla_p U(\mathbf{p}, \mathbf{x}). \tag{3.7}$$

The local disturbance velocity $\mathbf{u}$ satisfies the Stokes equation as described in section 2.2.2.

The last term in the rotational flux ($\dot{\mathbf{p}}$) equation corresponds to the nematic torque which leads to local alignment of particles. We define the tensor $\mathbf{D}$ as the second moment of the probability distribution function

$$\mathbf{D}(\mathbf{x}, t) = \int_S \Psi\mathbf{pp}\, d\mathbf{p}. \tag{3.8}$$

It is straightforward from Eq. (2.6) that the active stress tensor $\mathbf{\Sigma}^p = \sigma_0 \mathbf{D}$.

Following Doi and Edwards [4], we define the steric interaction energy U as

$$U(\mathbf{x}, \mathbf{p}, t) = \int_S \Psi(\mathbf{x}, \mathbf{p}', t)\beta(\mathbf{p}, \mathbf{p}')\, d\mathbf{p}', \tag{3.9}$$

with

$$\beta(\mathbf{p}, \mathbf{p}') = -U_0(\mathbf{p} \cdot \mathbf{p}')^2. \tag{3.10}$$

This function β is minimum when $\mathbf{p}$ and $\mathbf{p}'$ are aligned. So, a more nematically aligned suspension has a lower value of the steric interaction energy.

Substituting the expression for β from Eq. (3.10) in Eq. (3.9), the steric interaction energy simplifies to

$$U(\mathbf{x}, \mathbf{p}, t) = -U_0 \mathbf{pp} : \mathbf{D}(\mathbf{x}, t). \tag{3.11}$$

The nematic torque then takes the following form

$$\nabla_p U(\mathbf{x}, \mathbf{p}, t) = -U_0 \nabla_p(\mathbf{pp} : \mathbf{D}) = -2U_0(\mathbf{I} - \mathbf{pp}) \cdot \mathbf{D}(\mathbf{x}, t) \cdot \mathbf{p}, \tag{3.12}$$

so that equation (3.7) for $\dot{\mathbf{p}}$ becomes:

$$\dot{\mathbf{p}} = (\mathbf{I} - \mathbf{pp}) \cdot [\nabla_x \mathbf{u} + 2U_0 \mathbf{D}(\mathbf{x}, t)] \cdot \mathbf{p} - d\nabla_p(\log \Psi). \tag{3.13}$$

This equation for the rotational flux Eq. 3.13 shows that the orientation distribution in a concentrated suspensions is influenced by three effects.

- Steric interactions, which tend to align the particles towards a preferred direction, making the distribution more nematic.
- Hydrodynamic interactions, which tend to align the particles with the local disturbance flow.
- Rotational diffusion, which decorrelates the orientation and makes the distribution more isotropic

We use the same scales for non-dimensionalization as in 2.2.4. The dimensionless equations are obtained by letting $\mu = 1$, $V_0 = 1$, $\sigma_0 = \alpha$, $n = 1$, and having U_0, D, d and α as dimensionless parameters.

3.3 Existence of a nematic basestate

We know that, in passive rod suspensions there is a isotropic-nematic transition beyond a threshold concentration n^*. So, we try to find spatially uniform non-isotropic solutions to the basestate. We get this by setting the rotational flux to zero. This gives

$$\nabla_p \log(\Psi_{||}) = \xi(\mathbf{I} - \mathbf{pp}) \cdot \mathbf{D}(\Psi_{||}) \cdot \mathbf{p} \tag{3.14}$$

$\Psi_{||}$ is a boltzmann distribution obtained by the balance of rotational diffusion and steric interactions. ξ is a non-dimensional parameter describing the relative strength of steric interactions and rotational diffusion given by Eq .(3.15) (It should be noted that $\xi << 1$ corresponds to the semi-dilute regime) :

$$\xi = \frac{2U_0}{d} \tag{3.15}$$

In 2D, $\mathbf{p} = \mathbf{e}(\theta)$ and Eq. (3.14) becomes,

$$\partial_\theta \log(\Psi_{||}) = \xi \mathbf{e}_\perp \mathbf{e} \colon \mathbf{D}(\mathbf{\Psi}_{||}) \tag{3.16}$$

After some algebra this yields,

$$\Psi_{||} = \frac{\exp(\delta \cos 2\theta)}{\int d\theta' \exp(\delta \cos 2\theta)} \tag{3.17}$$

where

$$\delta = \frac{\xi}{4} \int d\theta' \Psi'_{||} \exp(\delta \cos 2\theta) \tag{3.18}$$

It is straightforward that $\delta = 0$, corresponds to the isotropic basestate. A nematic basestate exists if non-zero solutions for δ exist. Applying delta to both sides of the Eq. 3.17 we get

$$g(\delta) = \delta - \frac{\xi}{4} I(\delta) = 0 \tag{3.19}$$

$$\text{where} \qquad I(\delta) = \frac{\int_0^{2\pi} \sin\omega \exp(\delta \sin\omega) d\omega}{\int_0^{2\pi} exp(\delta \sin\omega) d\omega} = \frac{I_1(\delta)}{I_0(\delta)} \tag{3.20}$$

Fig. 3.2 (a) shows the plot of $g(\delta)$ for $0 < \xi < 16$. For small values of ξ, $g(\delta) = 0$ has only one solution, $\delta = 0$ (isotropic state). To find the zeros $\delta(\xi)$ of g, we use Newton's method. Fig. 3.2 (b) shows the roots of g as a function of ξ. We find that non-zero solutions for δ exist when ξ is above a critical value. The

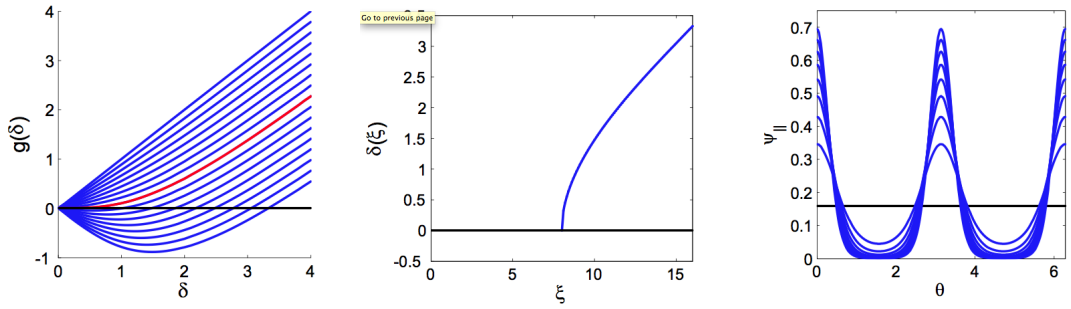

(a) (b) (c)

Figure 3.2: (a) $g(\delta)$ vs δ for $0 < \xi < 16$ (b) Roots of $g(\delta) = 0$ vs ξ (c) Nematic basestate profiles for different values of ξ

bifurcation of solution happens when $g'(0) \leq 0$. Eq. 3.23 shows that this happens when $\xi > 8$.

$$g(\delta) = \delta - \frac{\xi}{4}\frac{I_1(\delta)}{I_0(\delta)} \tag{3.21}$$

$$g'(\delta) = 1 - \frac{\xi}{4}\frac{I_0(\delta)I_2(\delta) - I_1(\delta)^2}{I_0(\delta)^2} \tag{3.22}$$

$$g'(0) = 1 - \frac{\xi}{4}\frac{d}{d\delta}\frac{I_0(\delta)I_2(\delta) - I_1(\delta)^2}{I_0(\delta)^2}\bigg|_{\delta=0} = 1 - \frac{\xi}{8} \tag{3.23}$$

$$\text{where } I_{j+1}(\delta) = I_j'(\delta) \text{and } I_j(\delta) = \int_0^{2\pi} \exp(\delta \sin\omega) \sin^j \omega d\omega \tag{3.24}$$

So, our analysis shows the existence of a isotropic-nematic transition in the basestate, when $\xi > 8$. So, $\xi < 8$ corresponds to the concentrated isotropic regime described in section 3.1 and $\xi > 8$ correspond to the liquid crystalline regime.

3.4 Numerical simulations

In this section, we perform numerical simulations of the kinetic equations discussed in section 3.2 in a three-dimensional periodic box of dimensions 50^3. We discretize using 64^3 grid points in the x, y, z directions and 16^2 grid points in the θ, ϕ direction. The probability distribution function $\Psi(\mathbf{x}, \mathbf{p}, t)$ becomes $\Psi(x, y, z, \theta, \phi, t)$ and the orientation vector is given by $\mathbf{p} = [\sin\theta\cos\phi, \sin\theta\sin\phi, \cos\theta]$.

As discussed in chapter II, the kinetic equations are integrated using spectral solutions for the Stokes equation, second-order finite differences for the flux terms and second-order Adams-Bashforth time-marching. We use the following parameters in our simulations: $\xi = 30$, $U_0 = 0.3$, rotational diffusion $d = 0.01$, translational diffusion $D = 1.0$, $\gamma = 1.0$. We choose a higher value of ξ to study the effect of steric

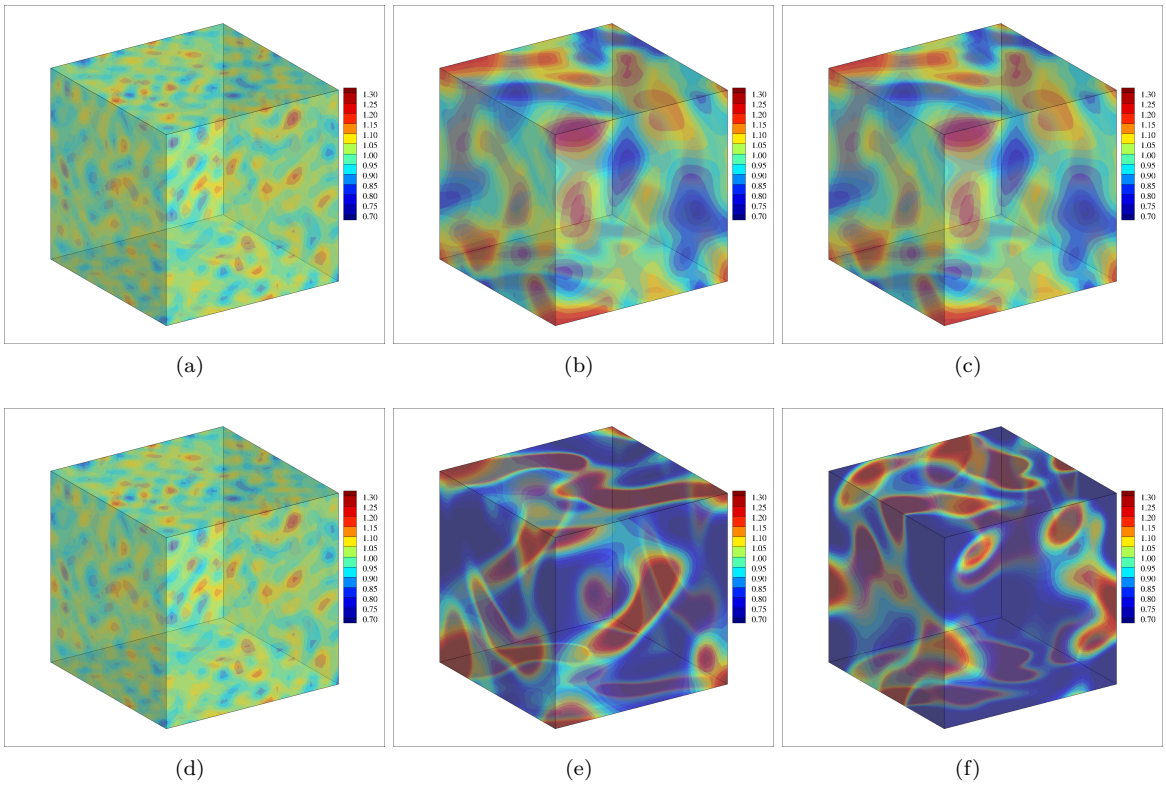

Figure 3.3: Number density field: a) $t = 0$, Pusher; b) $t = 150$, Pusher; c) $t = 300$, Pusher; d) $t = 0$, Puller; e) $t = 150$, Puller and f) $t = 300$, Puller.

interactions.

We start with a uniform and isotropic distribution and impose random perturbations and look at the evolution of the various fields. Interestingly, in our simulations, we observe instabilities and large scale flows for both pushers and pullers, while previous studies of semi-dilute active suspensions reported that puller suspensions were stable to perturbations from the isotropic state [2, 39]. This indicates that steric interactions have a destabilizing effect. To investigate this further, we look into the spatio-temporal fields to explore their evolution.

Fig. 3.3 shows the evolution of the number density. At t=0, the isotropic state is perturbed with random fluctuations. The fluctuations amplify and lead to the formation of dense clusters of active particle which form, deform and break up. These structures take the length of the simulation box. More interestingly, puller suspensions exhibit stronger number density fluctuations than pusher suspensions.

Now, to be able to study the effect of steric interaction, we find it useful to quantify alignment. As mentioned before, a lesser value of the steric interaction energy is indicative of a more aligned distribution. Therefore, the degree of alignment is directly proportional to the magnitude of the minimum of the steric

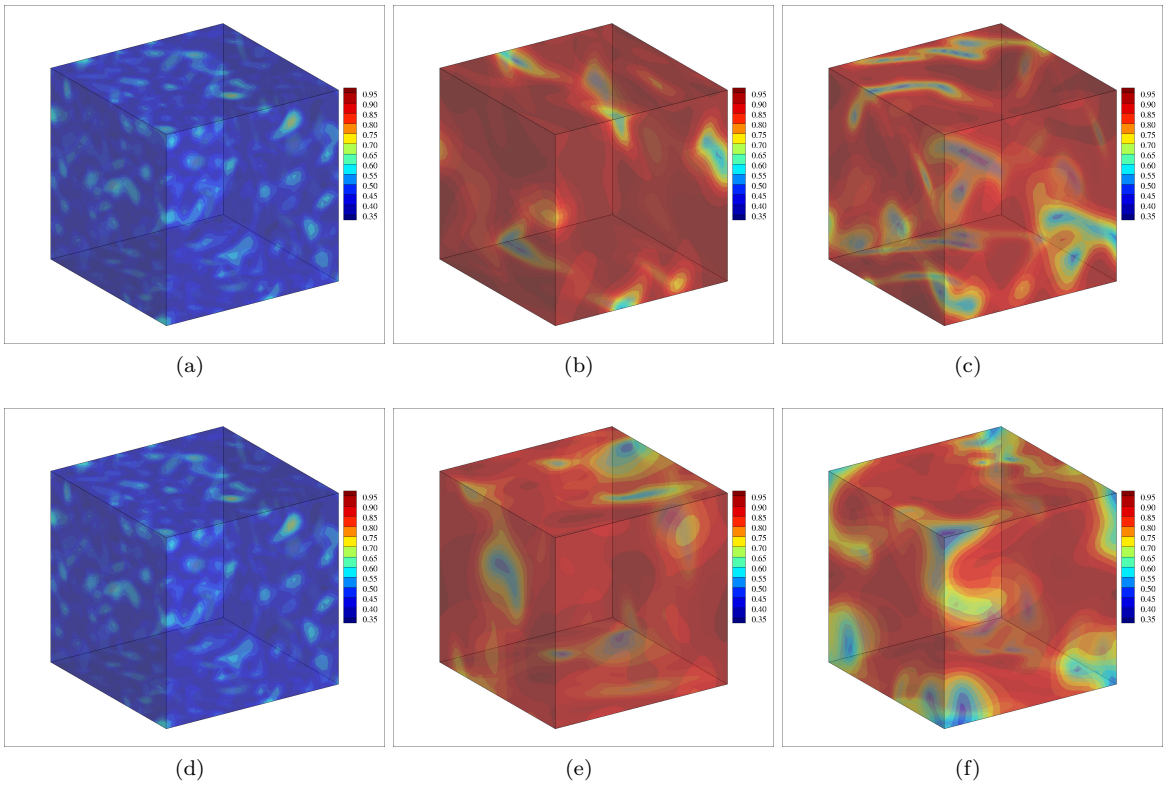

Figure 3.4: Degree of alignment field: a) $t = 0$, Pusher; b) $t = 150$, Pusher; c) $t = 300$, Pusher; d) $t = 0$, Puller; e) $t = 150$, Puller and f) $t = 300$, Puller.

interaction energy. We define the degree of alignment as,

$$N(\mathbf{x}, t) = -\frac{\min_p(U(\mathbf{x}, \mathbf{p}, t))}{U_0 c(\mathbf{x}, t)} = \frac{\alpha}{c(\mathbf{x}, t)} \tag{3.25}$$

where α is the eigen value of the probability distribution function. This can be shown to be $\frac{1}{3}$ for an isotropic distribution and 1 for a perfectly aligned distribution.

Fig. 3.4 shows the typical evolution of the degree of alignment for both pushers and pullers. It can be seen that perturbations to the initial isotropic state amplify and give rise to highly aligned structures (red regions indicate high degree of alignment). This is expected, as our simulations correspond to $\xi = 30$, where our theory predicts a transition to a spatially uniform nematic steady state. However, this state also develops spatio-temporal inhomogeneities for both pushers and pullers, which indicates that the nematic basestate is unstable. Regions of high degree of alignment form, and then they dealign and breakup, this happens because of an interplay between the steric interaction (which leads to orientation correlation), rotational diffusion (which leads to orientation decorrelation) and the hydrodynamic velocity (which leads to the nematic alignment of the particles with the flow).

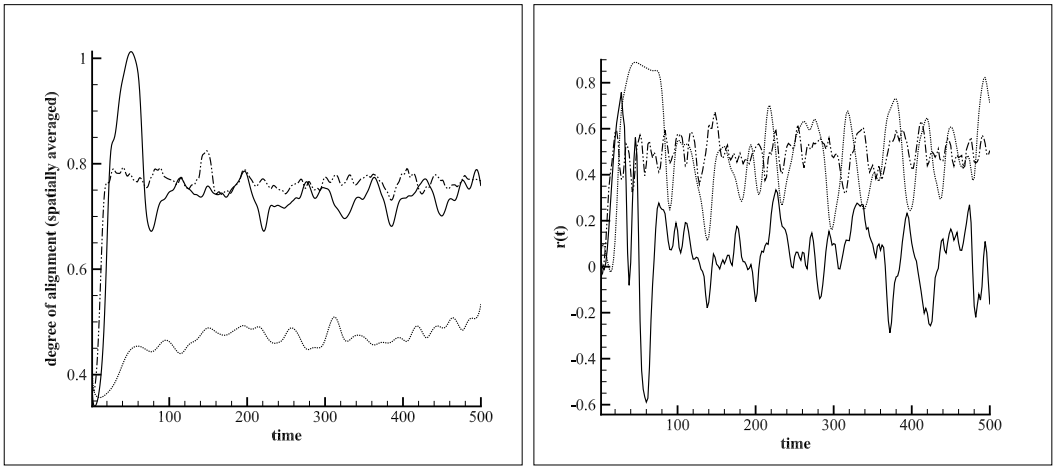

(a) (b)

Figure 3.5: a) Spatially averaged degree of alignment b) Correlation between degree of alignment and number density. Dotted line: semi-dilute pusher suspensions, Dasheddot line: concentrated pusher suspensions, Solid line: concentrated puller suspensions.

Fig. 3.5 (a) provides a better picture the evolution of degree of alignment in time. In concentrated pusher suspensions the distribution quickly becomes aligned, and reaches the statistical steady state value of 0.8. The fluctuations are indicative of the presence of instabilities. Concentrated puller suspensions reach a highly nematic state, and then become unstable. The semi-dilute pusher suspensions are shown for comparison. It can be seen that it reaches a statistical steady state value close to 0.4. So, the distribution is nearly isotropic for semi-dilute pusher suspensions, and the deviation from isotropy is because of the flow induced alignment.

We define a correlation between the degree of alignment and the number density as follows

$$\mathbf{r(t)} = \frac{\left\langle\, (c-1) \times (N - \langle N \rangle) \,\right\rangle}{\left(\left\langle\, (c-1)^2 \,\right\rangle \left\langle\, (N - \langle N \rangle)^2 \,\right\rangle\right)^{\frac{1}{2}}} \tag{3.26}$$

Fig. 3.5 (b) shows that the regions of high number density have a higher degree of alignment in pushers and this correlation is enhanced due to steric interactions. Puller suspensions show no such correlation.

We define the nematic director $\mathbf{d}_n(\mathbf{x}, t)$ as the preferred direction of nematic alignment. It is the unit vector along the direction which has the minimum steric interaction energy. It is straightforward to see that steric interaction energy is minimum when $\mathbf{p}$ is directed along the eigenvector of $\mathbf{D}$ (the second moment of the probability distribution) corresponding to the largest eigenvalue α.

Fig. 3.6 shows that the nematic director points in random directions initially, but as time evolves, the director becomes spatially correlated over length scales comparable to the size of the simulation box (for

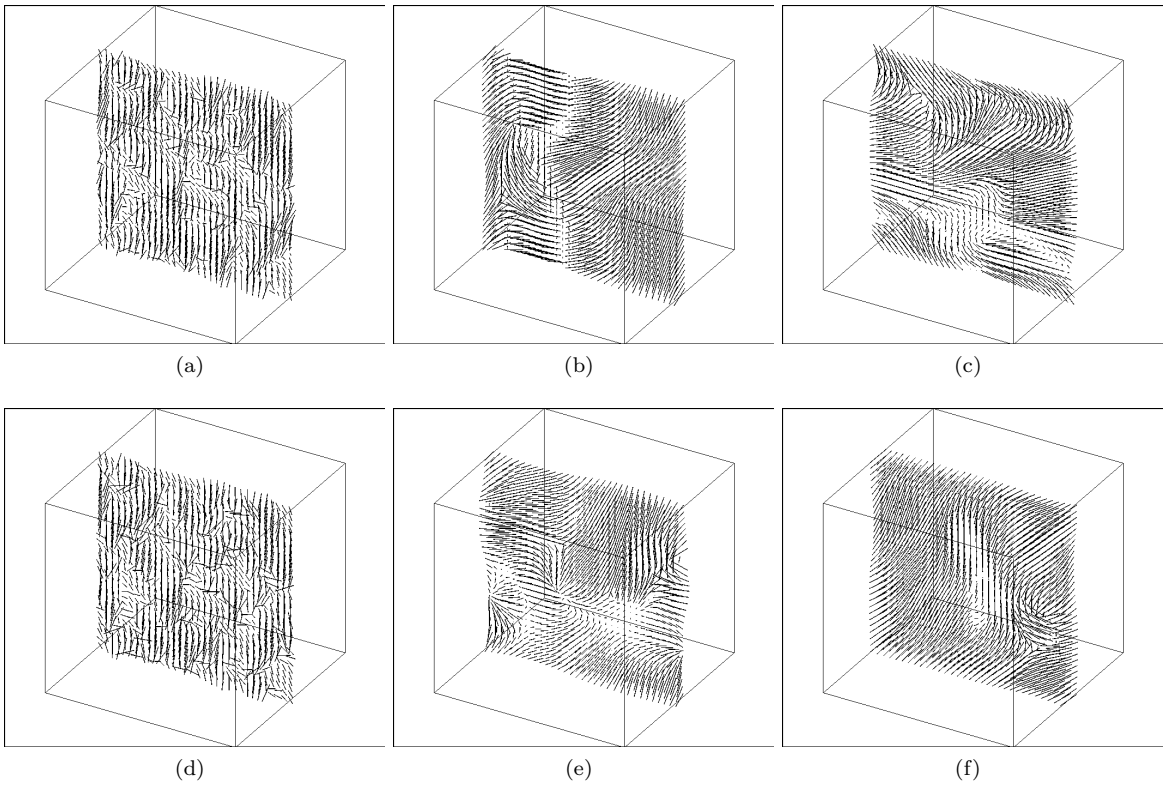

Figure 3.6: Nematic director: a) $t = 0$, Pusher; b) $t = 150$, Pusher; c) $t = 300$, Pusher; d) $t = 0$, Puller; e) $t = 150$, Puller and f) $t = 300$, Puller.

both pushers and puller). There is local ordering, and the direction of nematic alignment keeps fluctuating spatially and temporally. Fig. 3.7 shows the orientation distribution of the active particles at the random point (normalized by the concentration at that point). It can be seen that at longer times, the distribution becomes highly aligned about a particular direction, which is expected as the effect of the local alignment torque. This analysis reveals the existence of spatio-temporal fluctuations in the degree and the direction of nematic alignment in concentrated active suspensions.

However, the active particles that we consider here are polar. The self-propulsion of the active particles breaks the $(\mathbf{p}, -\mathbf{p})$ symmetry and leads to a net polarity in the system. It would be helpful to define a polar director:

$$\mathbf{d_p}(\mathbf{x}, t) = \frac{\int \mathbf{p}\Psi d\mathbf{p}}{\int \Psi d\mathbf{p}} \tag{3.27}$$

The polar director is the same as the mean direction of swimming of the active particles. The polar order parameter is simply the magnitude of the polar director $|\mathbf{d_p}(\mathbf{x}, t)|$. Saintillan and Shelley [2] showed that a net polarity is required for the creation of number density fluctuations and large scale flows in active

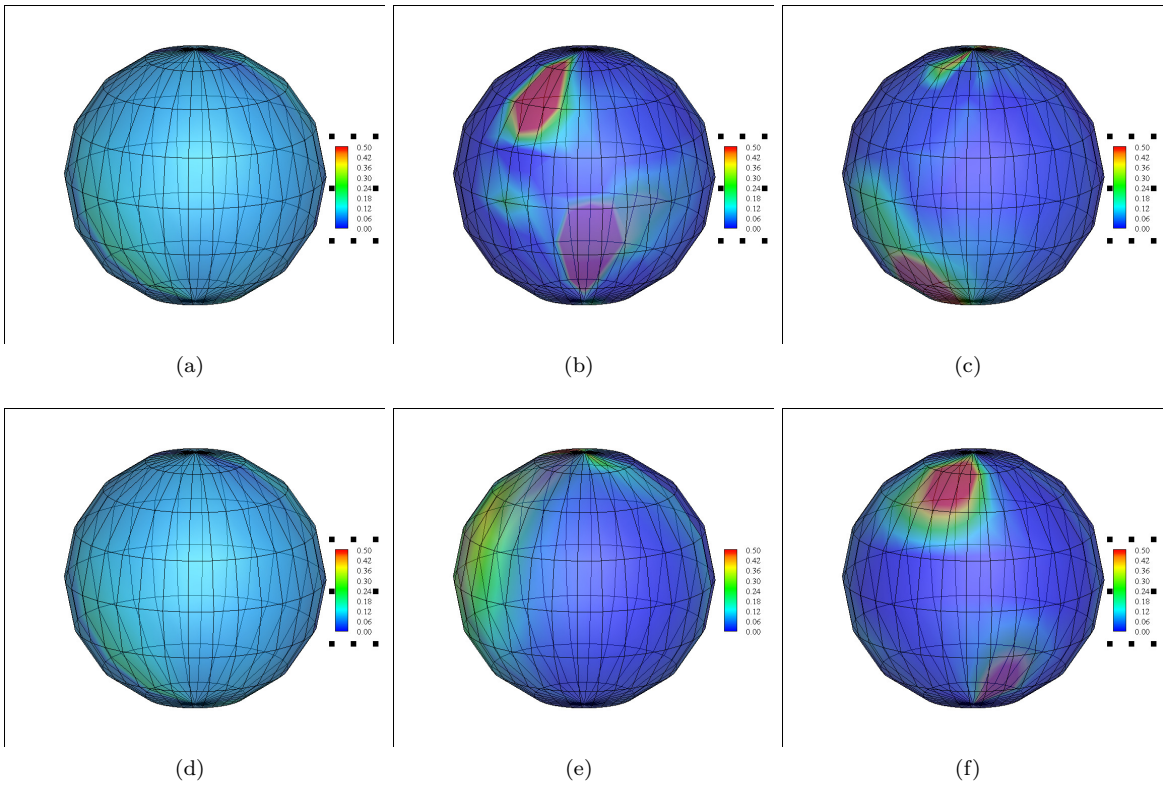

Figure 3.7: Distribution on a sphere of orientation at a random point: a) $t = 0$, Pusher; b) $t = 150$, Pusher; c) $t = 300$, Pusher; d) $t = 0$, Puller; e) $t = 150$, Puller and f) $t = 300$, Puller.

suspensions. By integrating the active particle conservation Eq. 3.5 over $\mathbf{p}$, we arrive at a conservation equation for the number density field $c(\mathbf{x}, t)$:

$$\frac{\partial c}{\partial t} + \mathbf{u} \cdot \nabla_{\mathbf{x}} c - D \nabla_{\mathbf{x}}^2 c = -\nabla_{\mathbf{x}} \cdot (c\, \mathbf{d}_p) \tag{3.28}$$

This equation clearly shows that a non-zero polarity is required for the number density fluctuations to grow. So, it is important to study the evolution of polarity and its correlation with hydrodynamic velocity and preferred direction of nematic alignment.

Fig. 3.8 (a) shows the time evolution of polar order parameter. A comparison of the semi-dilute and concentrated pusher suspension curves show that the polarity is slightly enhanced by steric effects. For pullers, the polarity at short times, decay because of the local disturbance velocity, but starts growing when the destabilizing steric interaction becomes dominant. The statistical steady state value of polar order parameter is higher for pullers than pushers. This explains why puller suspensions exhibit stronger number density fluctuations than pusher suspensions.

Fig. 3.8 (b) shows the time evolution of spatially averaged velocity magnitude. A comparison of semi-

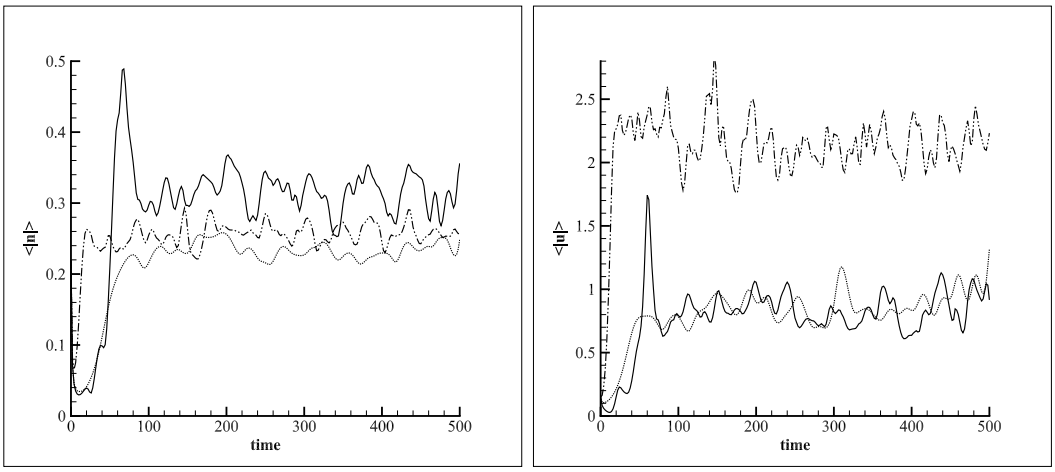

Figure 3.8: a) spatially averaged polar order parameter $\langle|\mathbf{d_p}(\mathbf{x},t)|\rangle$ b) spatially averaged velocity magnitude. Dotted line: semi-dilute pusher suspensions, Dasheddot line: concentrated pusher suspensions, Solid line: concentrated puller suspensions.

dilute and concentrated regimes is made to highlight the effect of steric interactions. It is clear that steric interactions lead to greater hydrodynamic velocities. Stronger hydrodynamic flows are created in concentrated pusher suspensions than concentrated puller suspensions.

In order to investigate the correlation between the polar director field $\mathbf{d}_p$, nematic director field $\mathbf{d}_a$ and velocity field $\mathbf{u}$ we use the spatially averaged contraction between any two fields, defined as

$$c_1(t) = \frac{1}{V}\int_V c(\mathbf{x},t)\mathbf{u}(\mathbf{x},t)\cdot\mathbf{d}_p(\mathbf{x},t)d\mathbf{x} \tag{3.29}$$

$$c_2(t) = \frac{1}{V}\int_V c(\mathbf{x},t)N(\mathbf{x},t)|\mathbf{u}(\mathbf{x},t)\cdot\mathbf{d}_n(\mathbf{x},t)|d\mathbf{x} \tag{3.30}$$

$$c_3(t) = \frac{1}{V}\int_V c(\mathbf{x},t)N(\mathbf{x},t)|\mathbf{d}_p(\mathbf{x},t)\cdot\mathbf{d}_n(\mathbf{x},t)|d\mathbf{x} \tag{3.31}$$

Fig. 3.9 (a) shows that the spatially averaged contraction of hydrodynamic velocity and polar director (mean direction of swimming) which is initially close to zero, and grows to reach a plateau with time. This net alignment is expected because the effect of the Jeffery's equation is to nematically align the active rods with the flow. More interestingly, it can also be seen from Fig. 3.9 (a) that pushers tend to nematically align in the local disturbance flow and swim along the direction of the flow. A comparison of the semi-dilute and concentrated pusher suspension curves leads us to a conclusion that steric interactions increases the tendency of the active particles to align and swim in the direction of the flow. (However, this might also be associated with increased magnitude of hydrodynamic velocities in the concentrated pusher suspensions

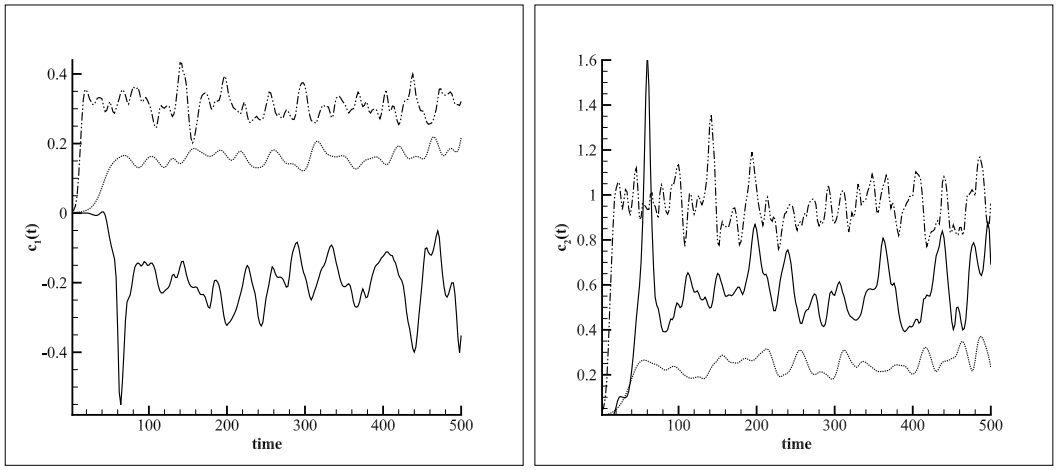

(a) (b)

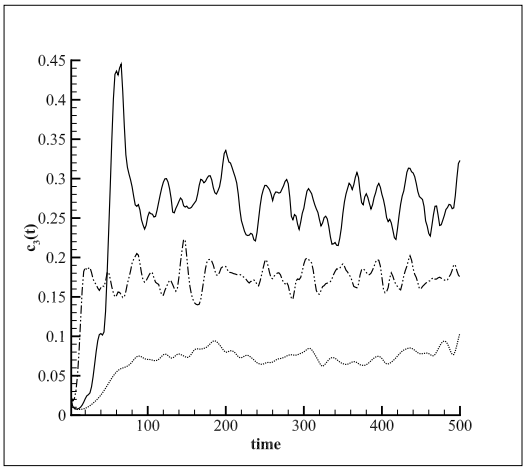

(c)

Figure 3.9: spatially averaged contraction of a) hydrodynamic velocity and polar director field b) hydrodynamic velocity and nematic director field c) polar and nematic director field. Dotted line: semi-dilute pusher suspensions, Dasheddot line: concentrated pusher suspensions, Solid line: concentrated puller suspensions.

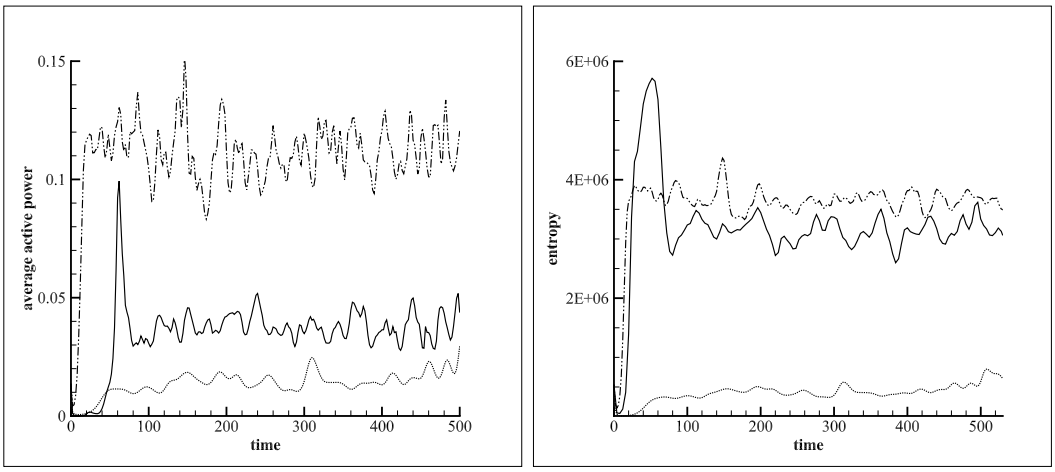

Figure 3.10: a) active input power b) Entropy Dotted line: semi-dilute pusher suspensions, Dasheddot line: concentrated pusher suspensions, Solid line: concentrated puller suspensions.

as observed in fig. 3.8 (b)). This preferred alignment and orientation result in an increase in the effective swimming velocity of the particles for pushers, a phenomenon already shown in some earlier works.

Pullers, on the other hand, align nematically with the local disturbance flow but swim anti-parallel to the direction of flow. This behavior leads to a decrease in the effective swimming velocity, and in regions where the swimming velocity is stronger than the polar director, the active particles effectively swim in a direction opposite to that of their self-propulsion. How this difference in alignment affects pushers and pullers needs further investigation.

Fig. 3.9 (b) and (c) shows that steric interactions lead to a better correlation of direction of steric alignment with both the hydrodynamic velocity and the polar director.

Following Saintillan and Shelley [2], we can find an interesting interpretation of the dynamics in terms of input power generated by the swimming particles. Therefore we define the local active power density as

$$p(\mathbf{x},t) = -\alpha \int_S (\mathbf{p} \cdot \ \mathbf{E} \cdot \mathbf{p}) \Psi(\mathbf{x},\mathbf{p},t)\, d\mathbf{p} \tag{3.32}$$

from which we can also define the global input power as $P(t) = \int_S p(\mathbf{x},t)\, d\mathbf{x}$.

Fig. 3.10 (a) shows that the total input power injected by the particles into the fluid increases and reaches a plateau over long times; The power injected increases because of the inclusion of steric interactions. Pushers injects more power into the fluid than pullers in the concentrated regime.

We define $S = \int d\mathbf{x} \int d\mathbf{p} \frac{\Psi}{\Psi_0} ln(\frac{\Psi}{\Psi_0})$ as the relative configurational average entropy where Ψ_0 is the probability density for the uniform and isotropic state. This is a positive semi-definite quantity which is zero for a uniform and isotropic distribution. So, this configurational entropy measures deviations from the

isotropic state. Fig. 3.10 reiterates the point that concentrated active suspensions form a state that is far from isotropy/nematic. The statistical steady state value of entropy in the concentrated regime is an order of magnitude higher than that in the semi-dilute regime.

3.5 Concluding Remarks

In this work, we proposed a model for concentrated active suspensions by extending the existing kinetic theory for the semi-dilute regime [1, 2], where we accounted for steric interactions by including a local alignment torque in the equation for rotational flux. Our analysis showed a basestate transition from isotropic to nematic, when ξ (a non-dimensional number measuring the relative strengths of steric interactions to rotational diffusion) becomes greater than 8. Three-dimensional kinetic simulations showed that both pusher and puller suspensions exhibit instabilities and large scale flows, hinting that steric interactions have a destabilizing effect qualitatively similar to that of hydrodynamic interactions in semi-dilute pusher suspensions. Degree and direction of nematic alignment and polarity were analyzed. Analysis of the fields showed several interesting details of the flow. Specially, pushers on average tend to swim along the local distribution velocity,creating an increase in overall swimming speed, while pullers swim against the local disturbance flow, creating a decrease in the overall swimming speed.

Chapter 4

Conclusions

In this work, we have considered two problems in active suspensions in which pattern formation and large scale flows have been reported in both experimental and theoretical studies. Our main aim was to understand how chemotaxis and steric interactions affect the collective behavior of these suspensions. Recent experiments [3, 5] were the main motivation to consider these effects.

In the first part of our work, we studied oxygentaxis in thin films of run-and-tumble bacteria, where recent experiments [3] show a transition to 3D behavior beyond a critical film thickness. Our three-dimensional simulations were successful in reproducing these experimental findings. In addition, we performed a detailed investigation of the spatio-temporal evolution of oxygen and bacterial fields which provides several new insights on the mixing of the oxygen field, consumption by the bacteria. We found it interesting to observe that no instabilities were found when oxygen coupling was removed, which show these instabilities are a combined result of oxygentaxis and hydrodynamic interactions. This also hints that confinement, run-and-tumble-dynamics have a stabilizing effect on the flow. This needs further investigation.

In the second part of our work, we focused on active suspensions in the concentrated regime, where we proposed a model that accounts for steric interactions. Our simulations showed instabilities characterized by number density fluctuations and large scale flows for both pushers and pullers. The degree and direction of alignment and polarity was quantified, the effect of steric interactions on the flow properties were discussed.

Both chemotactic and steric interactions have a destabilizing effect that is associated with their ability to align particles towards a preferential direction. In this respect, they have a qualitatively similar effect as hydrodynamic interactions in semi-dilute pusher suspensions. A more analytical description of these effects, say, using a linear stability analysis would present a even clearer picture.

References

[1] David Saintillan and Michael J. Shelley. Instabilities and pattern formation in active particle suspensions: Kinetic theory and continuum simulations. *Phys. Rev. Lett.*, 100(17):178103, Apr 2008.

[2] David Saintillan and Michael J. Shelley. Instabilities, pattern formation, and mixing in active suspensions. *Physics of Fluids*, 20(12):123304, 2008.

[3] Andrey Sokolov, Raymond E. Goldstein, Felix I. Feldchtein, and Igor S. Aranson. Enhanced mixing and spatial instability in concentrated bacterial suspensions. *Phys. Rev. E*, 80:031903, Sep 2009.

[4] M. Doi and S. F. Edwards. *The theory of polymer dynamics.* Oxford University Press, New York., 1986.

[5] Luis H. Cisneros, John O. Kessler, Sujoy Ganguly, and Raymond E. Goldstein. Dynamics of swimming bacteria: Transition to directional order at high concentration. *Phys. Rev. E*, 83:061907, Jun 2011.

[6] Tamas Vicsek. Universal patterns of collective motion from minimal models of flocking. In *Proceedings of the 2008 Second IEEE International Conference on Self-Adaptive and Self-Organizing Systems*, pages 3–11, Washington, DC, USA, 2008. IEEE Computer Society.

[7] Christopher Dombrowski, Luis Cisneros, Sunita Chatkaew, Raymond E. Goldstein, and John O. Kessler. Self-concentration and large-scale coherence in bacterial dynamics. *Phys. Rev. Lett.*, 93(9):098103, Aug 2004.

[8] Luis Cisneros, Ricardo Cortez, Christopher Dombrowski, Raymond Goldstein, and John Kessler. Fluid dynamics of self-propelled microorganisms, from individuals to concentrated populations. *Experiments in Fluids*, 43(5):737–753, 11 2007.

[9] N. Sambelashvili, A. W. C. Lau, and D. Cai. Dynamics of bacterial flow: Emergence of spatiotemporal coherent structures. *Physics Letters A*, 360:507–511, January 2007.

[10] Kyriacos C. Leptos, Jeffrey S. Guasto, J. P. Gollub, Adriana I. Pesci, and Raymond E. Goldstein. Dynamics of enhanced tracer diffusion in suspensions of swimming eukaryotic microorganisms. *Phys. Rev. Lett.*, 103:198103, Nov 2009.

[11] Xiao-Lun Wu and Albert Libchaber. Particle diffusion in a quasi-two-dimensional bacterial bath. *Phys. Rev. Lett.*, 84(13):3017–3020, Mar 2000.

[12] Neil H. Mendelson, Adrienne Bourque, Kathryn Wilkening, Kevin R. Anderson, and Joseph C. Watkins. Organized Cell Swimming Motions in Bacillus subtilis Colonies: Patterns of Short-Lived Whirls and Jets. *J. Bacteriol.*, 181(2):600–609, 1999.

[13] Andrey Sokolov, Igor S. Aranson, John O. Kessler, and Raymond E. Goldstein. Concentration dependence of the collective dynamics of swimming bacteria. *Phys. Rev. Lett.*, 98(15):158102, Apr 2007.

[14] Alfred Shapere and Frank Wilczek. Self-propulsion at low reynolds number. *Phys. Rev. Lett.*, 58(20):2051–2054, May 1987.

[15] Alfred Shapere and Frank Wilczek. Geometry of self-propulsion at low reynolds number. *Journal of Fluid Mechanics*, 198(-1):557–585, 1989.

[16] Juan P. Hernandez-Ortiz, Christopher G. Stoltz, and Michael D. Graham. Transport and collective dynamics in suspensions of confined swimming particles. *Phys. Rev. Lett.*, 95(20):204501, Nov 2005.

[17] David Saintillan and Michael J. Shelley. Orientational order and instabilities in suspensions of self-locomoting rods. *Phys. Rev. Lett.*, 99(5):058102, Jul 2007.

[18] T Ishikawa and T. J. Pedley. Diffusion of swimming model micro-organisms in a semi-dilute suspension. *Journal of Fluid Mechanics*, 588(-1):437–462, 2007.

[19] David Saintillan and Michael J. Shelley. Emergence of coherent structures and large-scale flows in motile suspensions. *Journal of The Royal Society Interface*, 2011.

[20] R. Aditi Simha and Sriram Ramaswamy. Hydrodynamic fluctuations and instabilities in ordered suspensions of self-propelled particles. *Phys. Rev. Lett.*, 89(5):058101, Jul 2002.

[21] John Toner, Yuhai Tu, and Sriram Ramaswamy. Hydrodynamics and phases of flocks. *Annals of Physics*, 318(1):170 – 244, 2005. Special Issue.

[22] Sumithra Sankararaman and Sriram Ramaswamy. Instabilities and waves in thin films of living fluids. *Phys. Rev. Lett.*, 102(11):118107, Mar 2009.

[23] Sriram Ramaswamy. The mechanics and statistics of active matter. *Annual Review of Condensed Matter Physics*, 1(1):323–345, 2010.

[24] Donald L. Koch and Ganesh Subramanian. Collective hydrodynamics of swimming microorganisms: Living fluids. *Annual Review of Fluid Mechanics*, 43(1):637–659, 2011.

[25] Pierre-Henri Chavanis. A stochastic keller-segel model of chemotaxis. *COMMUN.NONLINEAR SCI.NUMER.SIMULAT.*, 15:60, 2010.

[26] Tanvir Ahmed, Thomas Shimizu, and Roman Stocker. Microfluidics for bacterial chemotaxis. *Integr. Biol.*, 2:604–629, 2010.

[27] H Berg and R Anderson. Bacteria swim by rotating their flagellar filaments. *Nature*, 245(5425):380–382, 1973.

[28] T J Pedley and J O Kessler. Hydrodynamic phenomena in suspensions of swimming microorganisms. *Annual Review of Fluid Mechanics*, 24(1):313–358, 1992.

[29] N A Hill and T J Pedley. Bioconvection. *Fluid Dynamics Research*, 37(1-2):1, 2005.

[30] Evelyn F. Keller and Lee A. Segel. Model for chemotaxis. *Journal of Theoretical Biology*, 30(2):225 – 234, 1971.

[31] A. Hillesdon, T. Pedley, and J. Kessler. The development of concentration gradients in a suspension of chemotactic bacteria. *Bulletin of Mathematical Biology*, 57:299–344, 1995. 10.1007/BF02460620.

[32] G. Subramanian, Donald L. Koch, and Sean R. Fitzgibbon. The stability of a homogeneous suspension of chemotactic bacteria. *Physics of Fluids*, 23(4):041901, 2011.

[33] Ganesh Subramanian and Donald L. Koch. Critical bacterial concentration for the onset of collective swimming. *Journal of Fluid Mechanics*, 632(-1):359–400, 2009.

[34] G. B. Jeffery. The motion of ellipsoidal particles immersed in a viscous fluid. *Proceedings of the Royal Society of London. Series A*, 102(715):161–179, 1922.

[35] F. P. Bretherton. The motion of rigid particles in a shear flow at low reynolds number. *Journal of Fluid Mechanics*, 14(02):284–304, 1962.

[36] R. Bearon and T. Pedley. Modelling run-and-tumble chemotaxis in a shear flow. *Bulletin of Mathematical Biology*, 62:775–791, 2000. 10.1006/bulm.2000.0178.

[37] Kevin C. Chen, Roseanne M. Ford, and Peter T. Cummings. Cell balance equation for chemotactic bacteria with a biphasic tumbling frequency. *Journal of Mathematical Biology*, 47:518–546, 2003. 10.1007/s00285-003-0216-8.

[38] Amir Alizadeh Pahlavan and David Saintillan. Instability regimes in flowing suspensions of swimming micro-organisms. *Physics of Fluids*, 23(1):011901, 2011.

[39] Christel Hohenegger and Michael J. Shelley. Stability of active suspensions. *Phys. Rev. E*, 81(4):046311, Apr 2010.